Nuclear Science and Techniques (2026) 37:30
https://doi.org/10.1007/s41365-025-01849-3

Design and performance of the soft X-ray energy materials research beamline at SSRF

Zhen-Hua Chen[1] · **Li-Min Zhou**[1] · **Hai-Tao Li**[1] · **Ying Zou**[1] · **Yong Wang**[1] · **Ren-Zhong Tai**[1]

Received: 14 April 2024 / Revised: 14 October 2024 / Accepted: 16 October 2024 / Published online: 4 January 2026

Abstract
A soft X-ray energy materials research beamline (BL20U2), a branch of energy materials beamline (E-line), has been constructed in the Shanghai Synchrotron Radiation Facility (SSRF) Phase-II project. It is now operational for soft X-ray resonant emission spectroscopy (RXES) and soft X-ray resonant elastic scattering (REXS) investigations. Optical optimization was implemented for high performance, e.g., photon flux, energy-resolving power, and focus spot size. RXES experiments show that the energy range extends from 150 to 1500 eV. The elastic peak measured near titanium absorption edge (@445 eV) indicates an energy resolution of the RXES spectrometer of 65 meV. The measured photon flux is 3×10^{12} photons/s at 244 eV at the RXES sample position for an SSRF electron energy of 3.5 GeV and a projected ring current as 300 mA. The spot size at the RXES sample position is 23 μm in the horizontal direction and 7.9 μm in the vertical direction, respectively. Moreover, the angular resolution of elastic REXS scatterometer reaches 0.005° through measurement of X-ray reflection from the single-crystal silicon wafers. A sample of the REXS scatterometer is vibrationally decoupled from its chamber and cooled using copper braids connected from an open cycle liquid helium cryo reservoir, whereas the minimum sample temperature is below 15 K.

Keywords Synchrotron radiation · Materials research beamline · Wide-energy range · E-line · SSRF

1 Introduction

The Shanghai Synchrotron Radiation Facility (SSRF) is a third-generation medium-energy synchrotron radiation source, boasting excellent characteristics such as a wide wavelength range, high intensity, high brightness, collimation, polarization, and quasi-coherence. It facilitates groundbreaking research across diverse fields including life science, material science, environmental science, information science, condensed matter physics, and chemistry [1–5]. The key scientific challenges in energy development and utilization are inseparable from the development of materials science, particularly the need to understand, from a fundamental level [6]. The construction of a comprehensive research platform that combines a wide-energy range with multiple methods is vital to overcoming the limitations of characterization techniques and advancing in-depth research on energy material systems. The establishment of a wide-energy material beamline at SSRF can target the significant national energy strategy demands and support users in related fields to achieve significant scientific research results [7]. This beamline will address the diverse requirements of multiple disciplines and interdisciplinary fields. Herein, we report on the newly developed soft X-ray energy materials research beamline (BL20U2) in the SSRF Phase-II project [8], which is a branch of the energy materials beamline (E-line) [9]. BL20U2 at the SSRF comprises both a resonant emission spectroscopy (RXES) and a resonant elastic X-ray scattering (REXS) endstations. Herein, the RXES spectroscopy is suitable for revealing electronic characteristics including charge transfer (CT) during the redox process in the bulks or at the solid–liquid interfaces of battery materials, whereas the REXS scattering method can be applied to study and distinguish various spins, charges, orbitals, and lattice orders very directly.

✉ Ying Zou
zouy@sari.ac.cn

[1] Shanghai Synchrotron Radiation Facility (SSRF), Shanghai Advanced Research Institute, Chinese Academy of Sciences (CAS), Shanghai 201204, China

To date, several soft X-ray beamlines have been equipped with similar RXES or REXS spectroscopic endstations, including the RXES beamline at the Advanced Light Source (ALS) (beamline 8.0.1) [10] and those REXS beamlines at the Diamond light source [11], Stanford Synchrotron Radiation Light source (beamline 13-3) [12], and Canadian Light Source (REIXS Beamline) [13]. These beamlines have become critical implements for scientific research to elucidate electronic and magnetic states in energy materials.

Based on the demand of energy materials research and scientific characteristics, the design of the RXES spectrometer for beamline BL20U2 has adopted the basic configuration of the SLS spectrometer [14] but has been tailored to satisfy domestic scientific research demands. The parameters of the RXES spectrometer have been finely tuned for optimal performance, including grating type, length, curvature radius, grating line density, optimized energy point, entrance/exit arm length, charge-coupled device (CCD) pixels, and incident angle. The spectrometer operates in a wide-energy range of 150–1500 eV with a photon flux of 3×10^{12} photons/s@244 eV at the RXES sample position, operating energy of 3.5 GeV at SSRF, and expected ring current of 300 mA. The spot sizes are 23 μm and 7.9 μm in the horizontal and vertical directions, respectively, at the sample position of the RXES endstation. Meanwhile, the energy resolution of the RXES spectrometer reached 65 meV at the Ti absorption edge (445 eV), which is much larger than the design index of 90 meV. This enables resonance fluorescence emission [15, 16], CT [17, 18], d–d excitation [19, 20], multiplets [21], etc., to be investigated. Moreover, the first domestic soft X-ray REXS scatterometer, integrating six axis degrees of freedom for sample movement and three axis degrees of freedom for detector movement in an ultra-high vacuum environment, has been developed with reference to a CLS prototype scatterometer [22, 23]. The scatterometer with a minimum sample temperature as low as 15 K was achieved using copper braids cooling. Furthermore, an angular resolution of 0.005° degree was achieved, which is better than the design index of 0.01°.

2 Beamline

SSRF is a third-generation synchrotron with an electron energy of 3.5 GeV and low emittance of 3.9 nm · rad [24]. The elliptically polarized undulator (EPU) of BL20U2 has a period length of 60 mm, 30 periods, and a maximum *k*-value of 5.3, which can span a soft X-ray range from 130 to 1500 eV, covering the K-edge of nonmetal elements (B, C, N, etc.) and L-edge of most transition metals (Fe, Co, Ni, Mn, etc.) [25, 26].

2.1 Beamline design

The optical configuration of the BL20U2 beamline is shown in Fig. 1a. The main optical components are plane mirrors (SM1, SM2, and SM3a), elliptical cylindrical mirrors (SM5 and SM6), and a plane grating monochromator (PGM1). Figure 1b shows the site scene of the downstream optical hutch section of the beamline, whereby the beam comes in from lower left and passes through a mono-slit (exit slit), a post-focus mirror SM4, the REXS endstation, and a pair of post-focus KB mirrors (SM5/SM6), and reaches the RXES endstation at the terminus.

The beam emitted from the undulator propagates forward to a plane mirror, SM1, which is located at a distance

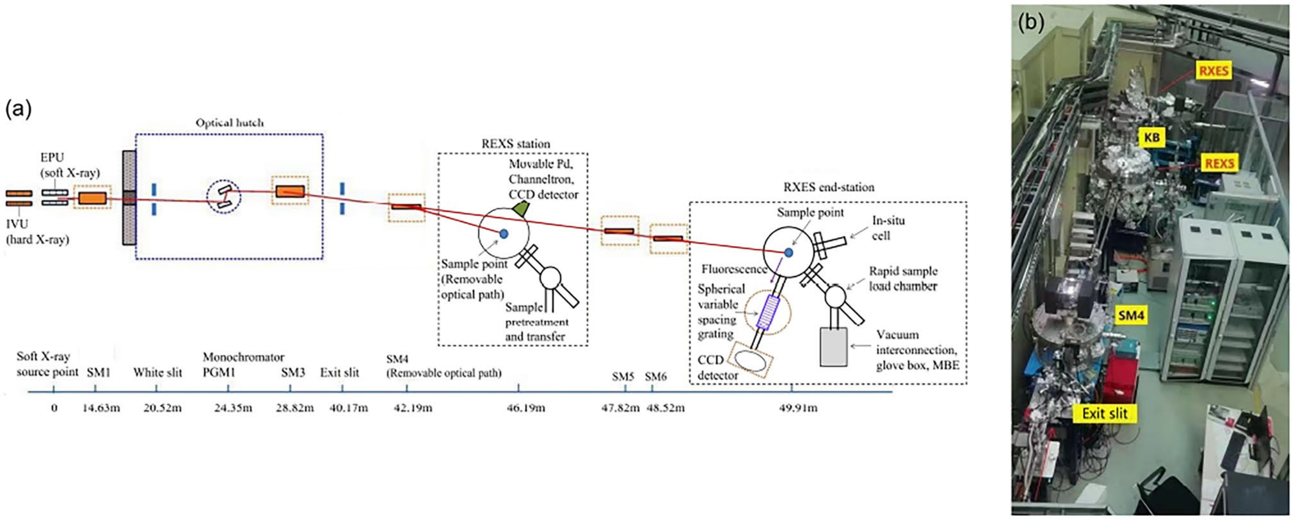

Fig. 1 (Color online) **a** Optical layout and **b** outside hutch site scene of the BL20U2 beamline

of 14.63 m relative to the center of the undulator. The grazing incidence angle of the beam on the first mirror SM1 is designed as 1.2° to generate a large angular offset and separate another hard X-ray branch away from our beamline [8]. To block the Bremsstrahlung induced by SM1, a piece of iron tungsten nickel alloy with a size of (120 mm (*H*)× 120 mm (*V*)× 50 mm (*L*)) is employed as a radiation blocking material in the safety shutter at the front end.

The monochromatization is based on a variable line spacing monochromator (PGM1) and an exit slit. Three holographically ruled gratings with central line densities of 300 , 800 , and 1200 L/mm were selected, whereas a variable included angle is achieved using a tilting mirror SM2 in the monochromator. The grating monochromator focuses the beam vertically to the exit slit at 40.17 m. A plane mirror SM3a downstream the monochromator, marked by an orange dashed box (Fig. 1a), deflects the beam outside the optical hutch to the experimental area. A toroidal mirror, SM4, was designed to be moved in or out of the path to refocus and deflect the beam to the REXS station or go straight downstream. The source of the SM4 mirror in horizontal direction locates at "0", which is at the center of the undulator, whereas the vertical source originates from the exit slit at 40.17 m. Both sources are imaged by the SM4 mirror onto the REXS sample position, 4 m downstream at 46.19 m. When the toroidal mirror SM4 is offline, the beam passes through the REXS chamber and be refocused by an elliptical cylindrical mirror SM5 in the horizontal direction and an elliptical cylindrical mirror SM6 in the vertical direction to the inelastic RXES endstation at 49.91 m. The source for the SM5 mirror in the horizontal direction is upstream at the center of the undulator, whereas the source for the SM6 mirror in the vertical direction is at the exit slit.

2.2 Beamline performance

The performance of the beamline including energy resolution, photon flux, energy range, and spot size at the RXES sample position is examined with the exit slit size set to 40 μm.

2.2.1 Energy range

The determination of photon energy range at BL20U2 is conducted by detecting the X-ray absorption near edge structure (XANES) of aluminum (Al). The Al 1 s peak is located at 1559.6 eV, and the Al 2 s peak is at 117.8 eV [27, 28]. The total electron yield (TEY) mode is employed to characterize the XANES spectra of a piece of single-crystal Al(100) at the RXES endstation. The TEY was measured under a ring current of 200 mA with a white slit size of 1000 μm × 3200 μm and an exit slit size of 40 μm. The acquisition scanning step for the spectra near the Al 1 s absorption peak is 0.25 eV, whereas the step near the Al 2 s absorption peak is 0.1 eV. The acquisition time is 1 s at each energy point. The 2 s absorption spectrum of Al with an absorption peak position of 118 eV is shown in Fig. 2a , whereas the Al 1 s absorption edge at 1560 eV is shown in Fig. 2b. These two measurements demonstrate the photon energy range is from 118 to 1560 eV, which exceeds that designed energy range between 130 and 1500 eV.

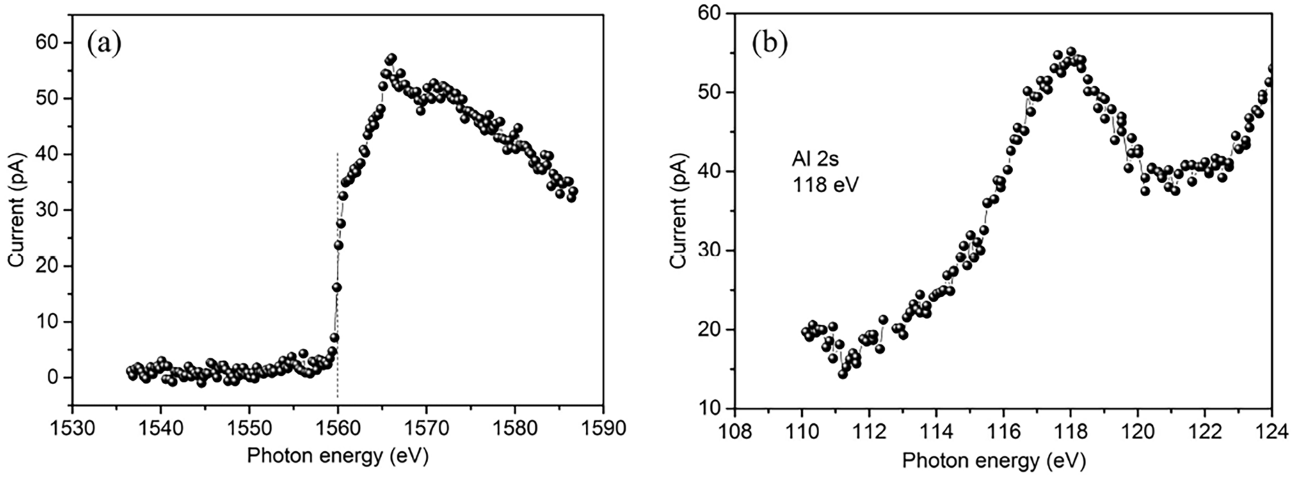

Fig. 2 TEY measurement of Al XANES features with the exit slit size at 40 μm. **a** Al 2 s absorption peak using 300 L/mm grating, **b** Al 1 s absorption peak using 800 L/mm grating

2.2.2 Energy resolution

An ionization chamber was installed downstream of the exit slit to measure the inner shell excitation spectra for standard gases, from which the beamline energy resolution can be obtained. The ionization chamber includes a vacuum cavity, leak valve with gas inlet, microchannel plate (MCP) detector, and nuclear electronics module (ORTEC 584/996) for amplifying and counting ion pulses [29, 30].

The advantage of such a setup is that gas core–shell ionization spectra can be measured under a very low working pressure such that collision broadening becomes negligible. In our experiments, the spectra were recorded for a gas pressure of 1×10^{-6} Torr with a white slit size of 1000 μm × 3200 μm and an exit slit size of 40 μm. The spectrum peak measured bears a Voigt profile: a natural life time broadened peak with a Lorentzian linewidth ΔL convolved by the beamline instrumental resolution with a Gaussian width ΔG.

Figure 3 shows the core–shell excitation spectra for Ar obtained using the 300 L/mm grating. The Ar $L_{2,3}$ absorption-edge transitions to the Rydberg levels $2p_{3/2} \rightarrow 4s, 3d, 4d, 5d, 6d$ and $2p_{1/2} \rightarrow 4s$ were all observed, as shown in Fig. 3a [31]. The $2p_{3/2} \rightarrow 4s$ transition ($h\nu =$ 244.39 eV) was used to characterize the energy resolution. The peak was simulated via a Voigt profile, assuming a Lorentzian linewidth $\Delta L = 112$ meV [32, 33] and Gaussian width of $\Delta G = 32.5$ meV as the beamline resolution was deconvolved. This yielded a resolving power of 7518 (relative energy resolution 1.33×10^{-4}), shown in Fig. 3b, which surpasses the designed resolving power of 5000.

2.2.3 Photon flux

The flux was measured under a synchrotron ring current of 200 mA. The photon flux at the expected RXES sample position was obtained using an AXUV100G photodiode, whose photocurrent, induced by its incident beam, is linearly proportionally to the flux. The EPU fundamental is tuned at 244 eV (near Ar $L_{2,3}$ edge), precisely at which the energy resolution was assessed. The scanning energy range is between 220 and 260 eV, with a white slit size of 1000 μm × 3200 μm, and an exit slit opening of 40 μm. The experimental photon current obtained for the 300 L/mm grating at the EPU fundamental's maximum is 2.81 μA, as shown in Fig. S1 (Supplementary Material). The photon flux can be calculated according to the photoelectric conversion efficiency of the photodiode, as shown in Eq. 1 [34]:

$$\text{Flux} = I \times 3.66 \times 300/(e \times I_{\text{BC}} \times \Delta E_{\text{beam}} \times 1000) \tag{1}$$

where I is the photocurrent (A) recorded by the photodiode at the sample position, e is the electron charge of 1.6×10^{-19}C, ΔE_{beam} is the energy broadening (eV) at 244 eV, and I_{BC} is the ring current (mA) during flux measurement. The calculated photon flux reduced to a ring current of 300 mA beam intensity at the RXES sample position is 3×10^{12} phs/s/0.1%BW, which is beyond the acceptance index of 2×10^{12} phs/s/0.1%BW.

2.2.4 Beam spot sizes at the RXES sample

The vertical size of the beam spot at a sample is an important factor in determining the energy resolution of the RXES spectrometer, which is designed to be better than 10 μm.

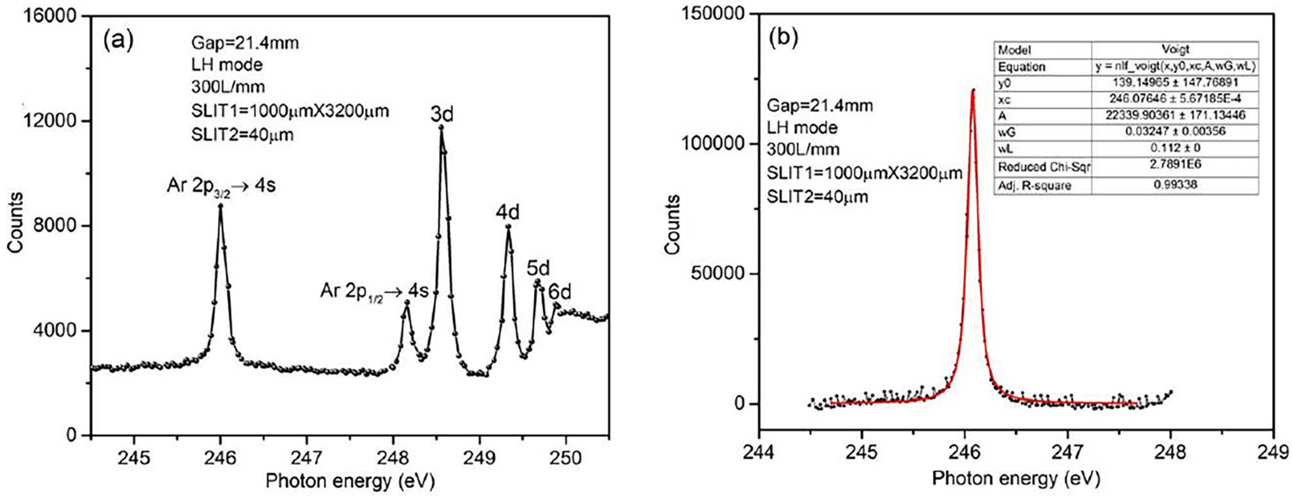

Model	Voigt
Equation	y = nlf_voigt(x,y0,xc,A,wG,wL)
y0	139.14965 ± 147.76891
xc	246.07646 ± 5.67185E-4
A	22339.90361 ± 171.13446
wG	0.03247 ± 0.00356
wL	0.112 ± 0
Reduced Chi-Sqr	2.7891E6
Adj. R-square	0.99338

Fig. 3 Ion yield spectra measured with the 300 L/mm grating. The opening for the exit slit is 40 μm. **a** Excitation spectra for Ar gas at the Ar L-edge from 244.5 to 250.5 eV. **b** The resolving power is 7518, as calculated from the $2p_{3/2}$-4 s transition peak. Color figure online

An X-ray beam position monitor (BPM) system has been installed at the RXES endstation and ready to measure the spot sizes at any time. This system consists of a bottom-mounted manipulator at the main chamber configured with a L-shaped blade and YAG:Ce scintillator and a downstream mounted AXUV100G photodiode. The YAG:Ce scintillator is employed to locate the X-ray beam position, whereas the photodiode is used to measure the photon intensity of direct soft X-ray beam.

The L-shaped blade is driven using stepper motors to scan across the beam spot at the supposed sample position, resulting in a step change of the intensity of photocurrent before and after shading. To obtain the spot profile in the horizontal or vertical direction, the step signal of the recorded photocurrent is taken as the first derivative, and the spot size is determined using its full width at half maximum (FWHM) value.

In our measurements, these scans were performed at 244 eV with a white slit size of $1000\,\mu\mathrm{m} \times 3200\,\mu\mathrm{m}$ and exit slit size of 40 μm under a ring current of 200 mA. The measured beam spot size at RXES endstation is 23 μm (*H*)× 7.9 μm (*V*), which is demonstrated in Fig. S2 (Supplementary Material). The vertical size (7.9 μm) is considerably smaller than the designed value for the RXES spectrometer, which indicates a superior performance of the RXES spectrometer at the BL20U2 beamline.

Next, we compare the performance of the designed soft X-ray energy material beamline with that of the international similar soft X-ray resonant inelastic scattering beamlines, such as beamline 8.0.1 at the ALS and the ADRESS beamline at the Swiss light source. Beamline 8.0.1 initially covers the photon energy range between 130 and 650 eV, enabling the study of emission spectra of sulfur, carbon, nitrogen, and oxygen atoms in battery materials, achieving a sufficient resolving power of $E/\Delta E \geq 1200$ [7]. The direct photon flux from the beamline monochromator is 10^{13} photons/s. At the sample position, the beam can be focused to a $100\,\mu\mathrm{m} \times 100\,\mu\mathrm{m}$ spot. In recent years, a high-throughput in-situ resonant inelastic X-ray scattering (iRIXS) endstation was developed at ALS beamline 8.0.1. The iRIXS endstation features two slit-less VLS spectrographs with different priorities on efficiencies, both featuring a wide operation energy range up to 1500 eV [12]. In addition, the ADRESS beamline at the Swiss light source covers the $0.4 - 1.8$ keV energy range. It has a high photon flux up to 10^{13} photons/s incident at the sample for a resolving power of approximately 12,000, which enables the detecting energy scale from that of CT and crystal field multiple excitations to that of collective orbital and magnetic excitations [35]. Compared with these beamlines, the constructed soft X-ray energy materials beamline has a wide-energy range (0.13 −1.5 keV) while also providing a decent photon flux (>3e12 cnts/s@244 eV) with a weighed up energy resolution ($\mathrm{RP} = E/\Delta E = 7518$). These features make the beamline suitable for studying electron excitation related process(e.g., CT or d–d excitation) in battery and catalytic materials.

3 RXES and REXS stations

3.1 RXES station

The RXES endstation primarily contains a sample main chamber and RXES spectrometer. The main sample chamber is a circular cavity with ultra-high vacuum standards, fabricated from SS316, and its base pressure is higher than 2×10^{-10} mbar. A low-temperature five-axis sample manipulator is top-mounted, with a variable temperature range of 10–500 K. The sample chamber is vacuum interconnected with a fast loading chamber backup using a glove box to offer a seamless sample loading for environmental sensitive samples. For enhanced efficiency of the fluorescence emission collection, two parabolic collection mirrors can be installed at the vicinity of the sample in the main chamber.

The RXES spectrometer is connected to the RXES sample chamber through its grating chamber. Soft X-rays irradiate the surface of samples at an incidence angle of 45°. The important geometric parameters of the RXES spectrometer include the length of the entrance arm (r_1), length of the exit arm (r_2), incident angle (α) and diffraction angle (β) of the grating, curvature radius (R) of the spherical grating, and CCD detector inclination angle (γ) (Refer to Fig. 4a). The entrance arm is at 80° to the incident X-ray and has a fixed length of one meter.

The RXES spectrometer adopts a configuration scheme of variable line spacing spherical gratings and a CCD detector [14]. The advantage of this scheme lies in fully utilizing the self-focusing characteristics of a variable line spacing grating to focus the fluorescence emitted by the sample on a focal plane, thereby effectively collecting the dispersive emission spectra in parallel using a CCD array detector with its detector plane coinciding with the focal plane, as shown in Fig. 4b.

According to the energy range and energy resolution requirements to be detected, three VLS gratings, referred as LEG, MEG, and HEG, with parameters as specified in Table 1, are employed to cover the photon energy range of 150 to 1500 eV. These parameters are optimized using the algorithm by Strocov [36] at energies of 225, 450 , and 900 eV, respectively. The central line density (a0) of each spherical grating is proportional to the reference optimized energy value such that the curvature radius of each remains unchanged, thereby the entrance arm of the spectrometer remains stationary to simplify the mechanical design of the RXES spectrometer.

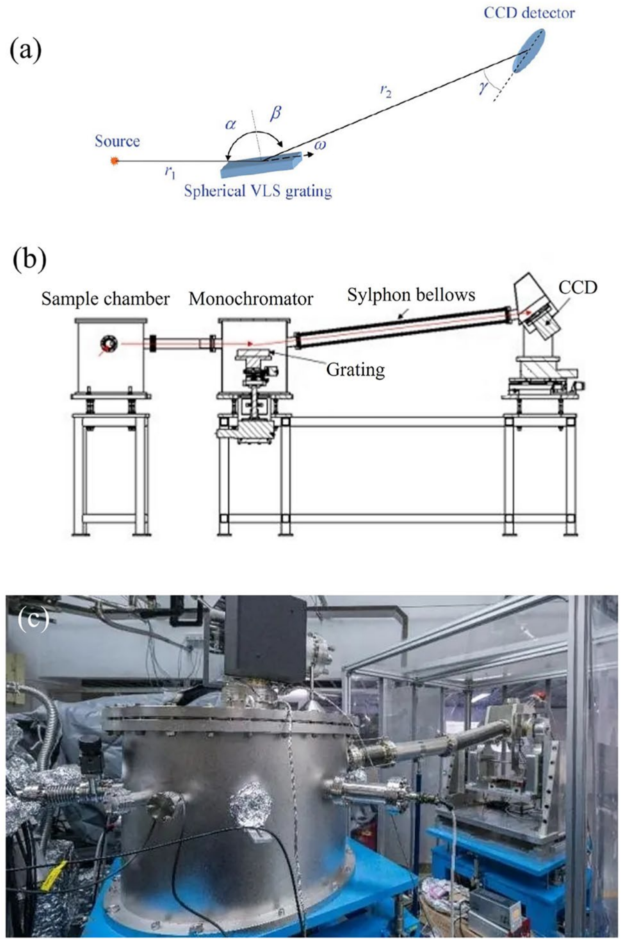

Fig. 4 **a** Conceptual representation of the RXES spectrometer. **b** Configuration or arrangement of the RXES spectrometer. **c** Photograph of the RXES spectrometer at the beamline BL20U2. Color figure online

Table 1 Main specifications of three varied line spacing gratings

Grating name	LEG	Item	
		MEG	HEG
Energy range (eV)	130–330	300–800	600–1500
Grating line density (L/mm)	600	1200	2400
Blaze angle (°)	1.4 ± 0.1	1.5 ± 0.1	1.6 ± 0.1
Curvature radius (mm)	41261.2	41261.2	41261.2

The incident grating angle is precisely optimized to minimize coma aberration at each energy, variable from 87.85° to 88.16° to cover the entire working energy range. Each grating is anticipated to have efficiencies of approximately 21%(LEG), 14%(MEG), and 7%(HEG), respectively, when operating at an incident angle of 88°. The dispersed light is allowed to propagate in the exit arm until it strikes the CCD camera. The length of the exit arm can vary from 1800 to 2130 mm to correlate the position of the CCD detector with the incident grating angle. The CCD detector has a device pixel size of 13.5 μm×13.5 μm and operates at an inclination angle of 20° to match the effective pixel size to the charge distribution caused by a single photon. Ultimately, the CCD is cooled to −70 °C, significantly reducing dark current to negligible levels. The entire spectrometer system, comprising the grating and CCD, is mounted onto a 3-m girder, as depicted in Fig. 4c. This configuration enables precise control over the vertical (Z motion) and transverse (X, Y motion) positioning of the spectrometer, ensuring accurate alignment with the scattered beam.

Various factors play important roles in determining the comprehensive energy resolution of the RXES spectrometer ($\Delta E_{\text{spectrometer}}$), such as the size of the beam spot incident on the sample, resolution of the spectrometer grating, lengths of the RXES spectral arms, and pixel size and aberration in the dispersion direction of the detector. During the spectrometer's design process, a theoretical energy resolution of 90 meV at 445 eV was proposed. In practice, the spectrometer energy resolution can be measured via the elastic peak of amorphous carbon film samples with bandless structures [37]. The total broadening of the elastic peak is formed by the convolution of the bandwidth of the beam line itself ($\Delta E_{\text{beamline}}$) and the energy resolution bandwidth of RXES spectrometer ($\Delta E_{\text{spectrometer}}$). Therefore, the energy resolution bandwidth of the spectrometer ($\Delta E_{\text{spectrometer}}$) can be obtained by subtracting the beam line bandwidth ($\Delta E_{\text{beamline}}$) from the peak width of the elastic peak (ΔE_{total}), as expressed in Eq. 2:

$$\Delta E_{\text{spectrometer}} = \sqrt{\Delta E_{\text{total}}^2 - \Delta E_{\text{beamline}}^2}. \tag{2}$$

The design index for ΔE spectrometer is set up for an energy of 445 eV because (1) it is near the absorption edge of titanium, one of the well-known transition metals used in oxide form as a photocatalyst; (2) it is close to the energy at which the MEG grating is optimized. Nevertheless, the beamline resolution at 445 eV has yet to be extrapolated out based on gas ionization spectra measured at 244 eV (Ar $2p_{3/2}$) and 401 eV(N 1 s) in the same manner as described in Sect. 2.2.2. The measurements were performed with a white slit size of 1000 μm × 3200 μm and exit slit size of 100 μm under a ring current of 200 mA. The derived beamline broadening values ($\Delta E_{\text{beamline}}$) are 56 meV(@244 eV) and 119 meV (@401 eV) using Voigt fitting, as shown in Fig. 5a and b. Herein, the beamline resolution at 445 eV is overestimated as 134 meV through extrapolation (Fig. 5c).

Next, we measured the elastic peak width of a carbon film sample with the RXES spectrometer at an incident photon energy of 445 eV (as shown in Fig. 6). A peak width of 4.95 pixels and a dispersion constant of 30 meV/pixel were recorded using the CCD detector, which provided a total broadening of 149 meV(ΔE_{total}). Through Eq. (3), the

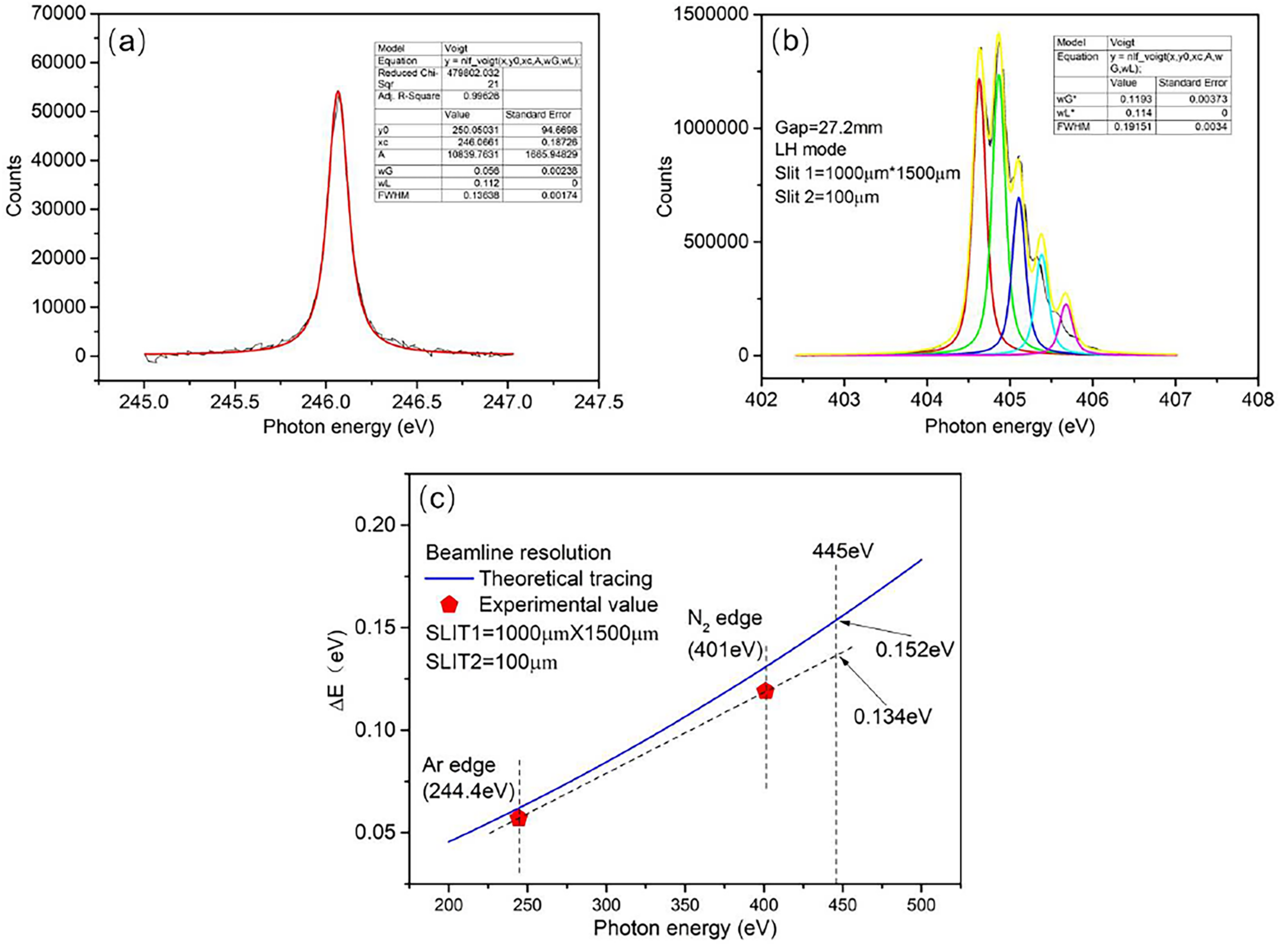

Fig. 5 Beamline resolution measurement (exit slit size of 100 μm) using **a** Ar gas ionization, the $2p_{3/2}$ absorption peak, and its Voigt fitting; **b** N_2 gas ionization, the 1 s absorption peak, and its Voigt fitting. **c** Based on the measured value in (**a**, **b**), linear extrapolated beamline resolution at 445 eV is 134 meV, overestimated compared with the theoretical ray tracing value (152 meV). Color figure online

beamline resolution has an overestimated value ($\Delta E_{\text{beamline}} = 134$ meV at 445 eV),

$$\Delta E_{\text{spectrometer}} = \sqrt{149^2 - 134^2} = 65\,\text{meV}. \tag{3}$$

The resolution bandwidth of the RXES spectrometer is conservatively estimated to be smaller than 65 meV, which is significantly superior to the desired resolution (90 meV@445 eV). As double-checking, the total broadening of the elastic peak at the incident photon energy of 401 eV was measured. A peak width of 4.90 pixels and dispersion constant of 29 meV/pixel were registered. This provides a total broadening of 142 meV. For a beamline resolution of 119 meV, directly measured using N_2 gas ionization at 119 meV, the resolution bandwidth of the spectrometer at 401 eV is calculated using Eq. 4,

$$\Delta E_{\text{spectrometer}} = \sqrt{142^2 - 119^2} = 77\,\text{meV}. \tag{4}$$

As a side note, this shows that for an energy (445 eV) close to the optimized energy point(450 eV), the resolution is greater than 77 meV. Moreover, the elastic peak at 244 eV (Ar L-edge) is depicted in Fig. 6d for the RXES spectrometer. The photon energy of the Ar L-edge was calibrated according its dispersion constant (Fig. 6e).

To demonstrate the functionality of the RXES spectrometer, Fig. 7 presents an XAS and RXES study for anatase TiO_2 nanocrystals. Figure 7a shows the Ti $L_{2,3}$ -edge XAS spectra of TiO_2 nanocrystals. The 3d-orbitals split into two different sublevels, t_{2g} and e_g, resulting from the spin orbit and other crystal field interactions, respectively. Moreover, the e_g sublevel undergoes an additional

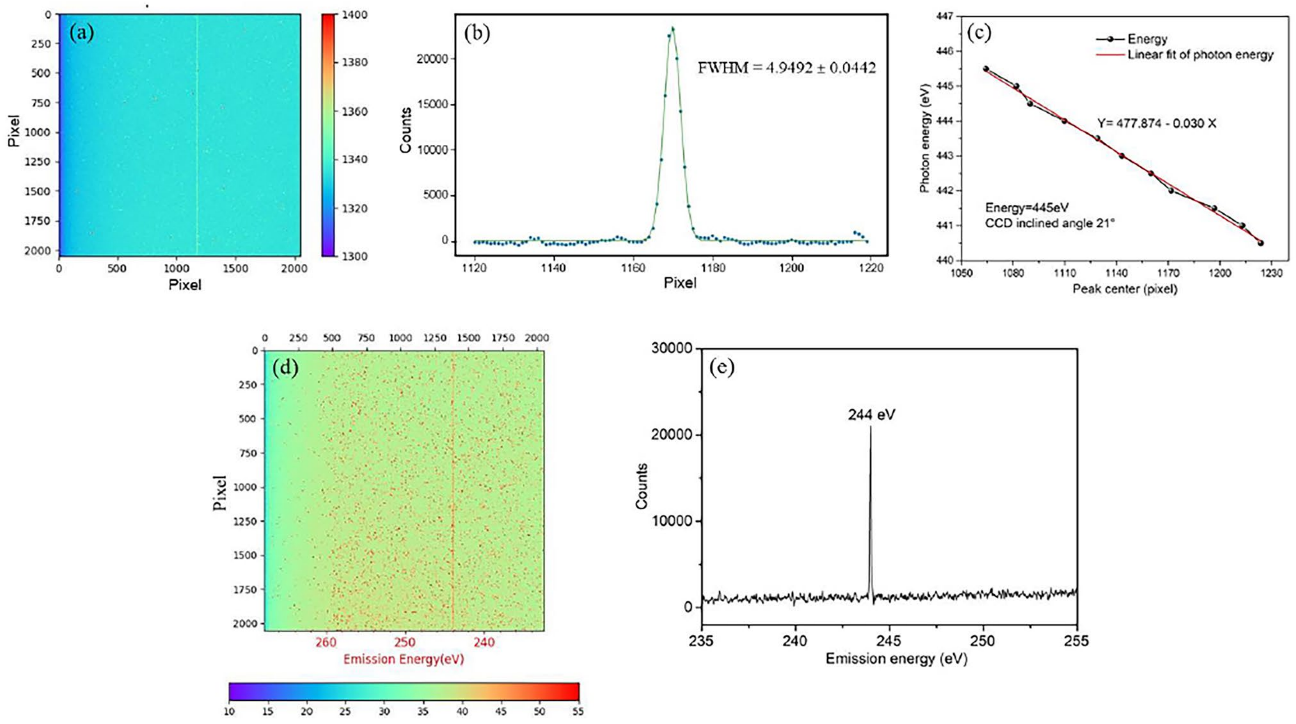

Fig. 6 (Color online) **a** Raw CCD mapping of the elastic peak from an carbon film measured using the RXES spectrometer at 445 eV with exit slit size of 100 μm. **b** Binned and Gaussian-fitted line spectrum of the elastic peak. **c** Dispersion constant measurement around 445 eV. **d** CCD mapping of the elastic peak at the Ar L-edge. **e** Calibrated photon energy at Ar L-edge (244 eV)

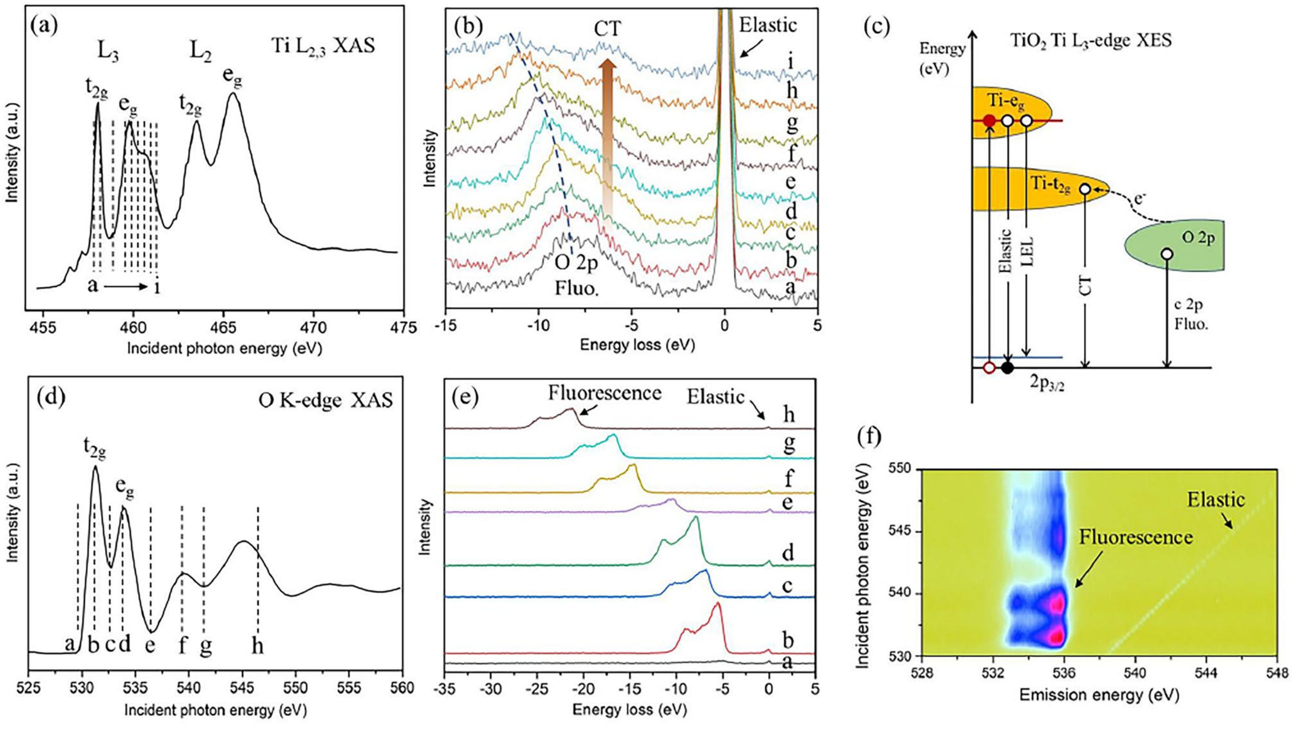

Fig. 7 (Color online) **a** TEY and **b** XES spectra obtained from different incident photon energy (**a**–**i**) of nanocrystals TiO_2 excited at Ti 2*p* threshold for the LV polarized configurations. **c** Schematic depiction of the Ti L_3-edge RXES process. **d** TEY and **e** XES spectra obtained from different incident photon energies (**a**–**h**) of TiO_2 excited at O 1*s* threshold. **f** O XES mapping near the O K-edge

asymmetric splitting at the Ti L_3-edge [37]. Incident X-rays with energies near the Ti L_3-edge (460 eV) excite the Ti 2p core electrons in the TiO_2 sample, which has a total angular momentum of 3/2, into unoccupied 3d states. The excited electrons can then relax via primarily three distinct channels, as demonstrated by the RXES processes (Fig. 7c). One is the direct deexcitation without energy loss, which results in an "elastic" peak (Fig. 7b). Another channel is inelastic deexcitation, producing a low energy loss (LEL, <1 eV) owing to certain charge-neutral elementary excitations such as magnons and polarons. Both elastic and LEL processes occur ubiquitously, independent of the existence of d electrons in the valence shell. Another channel involves an inelastic process, whereby other electrons with energies lower than the photoexcited electron may refill the 2p core hole instead. For the TiO_2 (Ti^{4+}) host lattice, after photoexcitation, electrons from the O 2*p* valence band may directly fill the Ti 2p core hole, emitting X-rays referred to as "O 2*p*" fluorescence [38]. Alternatively, an electron from adjacent O^{2-} ions can virtually hop into either the lower-energy t_{2g} or the higher-energy e_g subshell of Ti^{4+} through a CT process. Subsequently, this electron may undergo decay in place of the photoexcited electron. Because both the O 2*p* fluorescence and CT process require large additional energy costs, they manifest in the RIXS spectrum within a high energy-loss region (4 – 11 eV, see Fig. 7b). A schematic depiction of the deexcitation details in the Ti L_3-edge RXES process is shown in Fig. 7c.

The features observed in the O K-edge XAS of the TiO_2 in the TEY mode (Fig. 7d) can be interpreted by the splitting of the 3*d* states, t_{2g} and e_g orbitals, which correspond to electronic transitions from the O 1*s* orbital to a covalently mixed state derived from the O 2p and Ti 3d states of TiO_2, whereas the broader bands located between 536 eV and 550 eV are related to transitions between the O 2*p* and Ti 4*sp* hybrid bands. The crystal field strength is defined as the energy difference between t_{2g} and e_g orbitals in the TiO_2. Generally, the e_g orbitals are more easily affected by the local environment than the t_{2g} bands [39]. Figure 7e shows RXES features of fluorescence peaks from the Ti_{3d}–O_{2p} and Ti_{4sp}–O_{2p} states near the O K-edge in TiO_2 sample, corresponding to a decay from the relatively broad (delocalized) oxygen valence band states to fill the excited O1*s* core hole. The RXES intensity map presented in Fig. 7f is plotted with incident photon energy in the *y*-axis (the same as the *x*-axis in the XAS plot) against the emission energy in the *x*-axis.

The RXES sample manipulator is equipped with a LHe-cryostat and cartridge heater (Lakeshore HTR-25-100). In actual operation, this configuration enables the sample temperature to be variable from a base tested temperature of 7.276 K to a high elevated temperature of 803 K (Fig. S3 in Supplementary Material), which surpasses the designed temperature range of 10–500 K.

3.2 REXS station

REXS has emerged as a probing method with unique sensitivities to spin, charge, and orbital long range order [40–44]. The key of the technique is to combine X-ray spectroscopy, a probe of electronic structure, with X-ray diffraction, a probe of spatial order. Through tuning the energy of X-ray to specific X-ray absorption edges, X-ray scattering can be made very sensitive to particular atomic orbitals of an element. This makes REXS valuable sensitive not only to specific elements but also to specific atomic orbitals (e.g., O 2*p* or Cu 3*d* states) of a given element, as well as the spin and symmetry of those orbitals (e.g., the projected O 2*px* states).

This REXS experimental station at the BL20U2 beamline is primarily composed of an ultra-high vacuum chamber, in-vacuum scatterometer, sample holder with cryostat, and vacuum interconnection system for sample transfer (Fig. 8). Among them, the core part is a four-circle UHV scatterometer with a total of nine degrees of motion. The scatterometer has a full range of θ and 2θ motions, each spanning −20° to 170°, and limited χ and ϕ motions, each spanning ±4.5°. In addition, the sample position can be moved ±7.5 mm in the *x*, *y*, and *z* directions to position a sample into the center rotation of the scatterometer. In addition to these seven motions, the detector arm enables a height adjustment of 90 mm to position any of the three detectors (a photodiode, channeltron, and CCD detector) into the horizontal scattering plane. A slit wheel with unlimited 360° rotation enables any one of ten slits to be positioned in front of the channeltron. All of these motions are achieved using in-vacuum stepper motors. Either θ or 2θ motion provides a designed precision greater than 0.01°.

For alignment adjustment and vibration isolation during the measurement process, the three stainless steel support screws at the bottom of the scatterometer are connected to the vacuum chamber through bellows to isolate the vibration passed on by the chamber wall. The three screws are fixed on a stainless steel chassis as a whole, and the chassis can be adjusted in two dimensions in the *x* and y directions within a range of ±2.5 mm and can move within a range of ±10 mm in the vertical direction (*z*), ensuring θ and 2θ axis of the turntable intersects vertically with the beam of incident X-ray beam.

To test the rotation resolution of the in-vacuum REXS scatterometer, we trace the motion of the reflection peak of silicon wafer near 20° on the CCD camera upon θ axis jogging. Each jogging rotates the sample rotation axis (θ) with a fixed step of angular degree of 0.005°. The full test includes jogging in the same direction continuously more

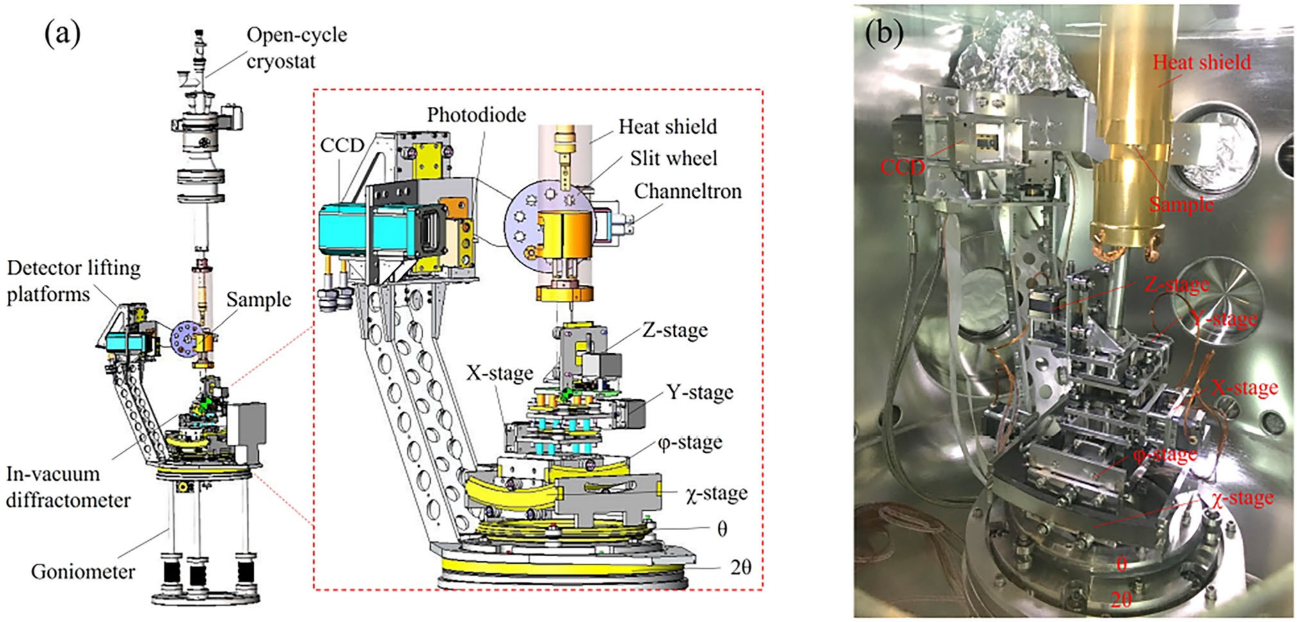

Fig. 8 (Color online) **a** Schematic of the REXS in-vacuum scatterometer. **b** Photograph of the REXS scatterometer at BL20U2

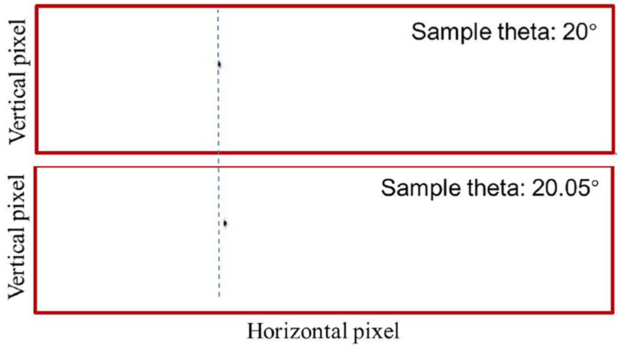

Fig. 9 Comparison of the positions of reflected beam on the CCD format before and after ten theta joggings

Table 2 Pixel position and crossed pixels of the reflected beam upon single θ jogging as tabulated, the average crossed pixel is 1.34 ± 0.13

Sample rotation (°)	Item	
	Pixel position (pixel)	Crossed pixels (pixel)
20	323.98	
20.005	325.29	1.31
20.01	326.73	1.44
20.015	328.12	1.39
20.02	329.66	1.54
20.025	330.96	1.3
20.03	332.25	1.29
20.035	333.38	1.13
20.04	334.81	1.43
20.045	336.02	1.21
Average crossed pixel		1.34 ± 0.13

than five times. At each position, the CCD detector is used to capture the reflection peak image, and the angle distribution is determined by binning or segmenting data along the vertical axis. The position of peak (pixel position) is fitted to obtain the number of crossed pixels, PX, upon each jogging. When $\mathrm{PX} \geq 1$, the rotation resolution 0.005° is considered to be reached.

The measurements were performed at 244 eV with the CCD exposure time set as 1 s, a white slit size of 200 μm× 200 μm, and an exit slit size of 40 μm under a ring current of 200 mA. Figure 9 compares the positions of the reflected light spot on the CCD format before and after ten joggings; correspondingly, the detailed pixel position/crossed pixels of each jogging with a step size of 0.005° are tabulated in Table 2. From the test results, the average number of crossed pixels, $\mathrm{PX} = 1.34$, is greater than 1 pixel. This showed that a minimum jogging size of 18 arcseconds (0.005°) was achieved. Therefore, we obtained a rotation resolution of 0.005° for the REXS sample axis, which surpasses the design index of 0.01°.

The temperature of the sample holder is monitored and controlled using two silicon diode temperature sensors (Lakeshore DT-670B-SD), with one sensor close to the sample position and a second one on the second stage of the cryostat. The sample is heated using a 25 Ω 100 W cartridge heater (Lakeshore HTR-25-100) located above the sample position. This heater is thermally connected but electrically isolated from the sample receptacle using a sapphire plate and ceramic hat washers. This is performed to eliminate leakage currents from the heater to avoid errors in the TEY absorption measurements by sample drain current. This configuration of the heater enables the sample temperature to be increased from a base tested temperature of 14.837 K up to a high elevated value of 500.27 K (Fig. S4 in Supplementary Material), which surpasses the designed temperature range of 10–500 K.

4 Summary

The BL20U2 soft X-ray energy materials beamline at SSRF has been constructed for inelastic RXES and elastic REXS experiments. The beamline is optimized by using two sets of post-focus mirrors for the two different experimental station to ensure high performance. The beamline has a wide working energy range of $130-1500\,\mathrm{eV}$. The tested photon flux at 244 eV is 3×10^{12} photons/s with a resolving power 7519 at the RXES sample position for the SSRF electron energy of 3.5 GeV and an expected ring current of 300 mA. The RXES endstation measures a spot size of 23 μm horizontally and 8 μm vertically. Meanwhile, the energy resolution of RXES spectrometer was verified as 65 meV at the Ti absorption edge (445 eV), which enables the study of fluorescence emissions, CTs, and d-d excitations or multiples. A variable temperature of RXES sample stage range from 7.276 K to 803 K has been achieved, which surpasses the designed temperature range of 10–500 K. Moreover, the first domestic soft X-ray REXS scatterometer, integrating six axis degrees of freedom of sample movement and three axis degrees of freedom of detector movement in an ultra-high vacuum environment, has been developed. A controllable sample temperature range of 14.837–500.27 K has been achieved. A rotation resolution of 0.005° was confirmed at the scatterometer, which enables the REXS endstation to be used to study and distinguish between various spins, charges, orbitals, and lattice orders very directly and in considerable detail.

Supplementary Information The online version contains supplementary material available at https://doi.org/10.1007/s41365-025-01849-3.

Author's contributions All authors contributed to the study conception and design. Material preparation, data collection and analysis were performed by Zhen-Hua Chen, Li-Min Zhou, Hai-Tao Li and Ying Zou. Supervision was performed by Yong Wang and Renzhong Tai. The first draft of the manuscript was written by Zhen-Hua Chen, and all authors commented on previous versions of the manuscript. All authors read and approved the final manuscript.

Data availability The data that support the findings of this study are openly available in Science Data Bank at https://cstr.cn/31253.11.sciencedb.j00186.00743 and https://www.doi.org/10.57760/sciencedb.j00186.00743.

Declarations

Conflict of Interest Ren-Zhong Tai is an editorial board member for Nuclear Science and Techniques and was not involved in the editorial review, or the decision to publish this article. All authors declare that there are no Conflict of interest.

References

1. G. Jiao, S. Tian, S. Xiang et al., Installation and commissioning of accelerators associated with the new beamline in synchrotron radiation light source. Nucl. Tech. (in Chinese) **47**, 030101 (2024). https://doi.org/10.11889/j.0253-3219.2024.hjs.47.030101
2. K. Liao, Z. Xu, L. Zhao et al., Development of a grazing incidence X-ray diffractometer for BL02U2 at SSRF. Nucl. Tech. (in Chinese) **46**, 120101 (2023). https://doi.org/10.11889/j.0253-3219.2023.hjs.46.120101
3. Z. Qiu, K. Li, H. Xie et al., Study of 20 Hz high spatial-temporal resolution monochromatic X-ray dynamic micro-CT. Nucl. Tech. (in Chinese) **46**, 070101 (2023). https://doi.org/10.11889/j.0253-3219.2023.hjs.46.070101
4. X. Liu, S. Tian, X. Wu et al., Intra-beam scattering and beam lifetime in a candidate lattice of the soft x-ray diffraction-limited storage ring for the upgraded SSRF. Nucl. Sci. Tech. **32**, 83 (2021). https://doi.org/10.1007/s41365-021-00913-y
5. F. Zhu, J. Cao, X. Meng et al., Spatial- and spin-resolution ARPES and magnetism beamline at SSRF. Nucl. Sci. Tech. **35**, 130 (2024). https://doi.org/10.1007/s41365-024-01484-4
6. H. Zhang, L. Xie, Z. Liang et al., Tandem catalysis for enhanced CO oxidation over the Bi–Au–SiO_2 interface. Nucl. Sci. Tech. **34**, 108 (2023). https://doi.org/10.1007/s41365-023-01256-6
7. Z. Chen, F. Sun, Y. Zou et al., Design of wide-range energy material beamline at the Shanghai synchrotron radiation facility. Nucl. Sci. Tech. **29**, 26 (2018). https://doi.org/10.1007/s41365-018-0356-6
8. R.Z. Tai, Z. Zhao, Overview of SSRF phase-II beamlines. Nucl. Sci. Tech. **35**, 137 (2024). https://doi.org/10.1007/s41365-024-01487-1
9. B. Mei, L. Wang, S. Gu et al., A seven-crystal spectrometer for high-energy resolution x-ray spectroscopy at Shanghai synchrotron radiation facility. Nucl. Sci. Tech. **35**, 156 (2024). https://doi.org/10.1007/s41365-024-01486-2
10. L. Weinhardt, M. Blum, O. Fuchs et al., RIXS investigations of liquids, solutions, and liquid/solid interfaces. J. Electron Spectrosc. **188**, 111–120 (2013). https://doi.org/10.1016/j.elspec.2012.10.006
11. T.A.W. Beale, T.P.A. Hase, T. Iida et al., RASOR: an advanced instrument for soft x-ray reflectivity and diffraction. Rev. Sci. Instrum. **81**, 073904 (2010). https://doi.org/10.1063/1.3458004
12. J. Fink, E. Schierle, E. Weschke et al., Resonant elastic soft x-ray scattering. Rep. Prog. Phys. **76**, 056502 (2013). https://doi.org/10.1088/0034-4885/76/5/056502
13. B.Y. Pan, H. Jang, J.S. Lee et al., Intertwined spin and orbital density waves in MnP uncovered by resonant soft X-ray scattering. Phys. Rev. X **9**, 021055 (2019). https://doi.org/10.1103/PhysRevX.9.021055
14. V. Strocov, Concept of a spectrometer for resonant inelastic x-ray scattering with parallel detection in incoming and outgoing photon energies. J. Synchrotron Radiat. **17**, 103–106 (2010). https://doi.org/10.1107/S0909049509051097

15. Y.D. Chuang, X. Feng, P.A. Glans-Suzuki et al., A design of resonant inelastic X-ray scattering (RIXS) spectrometer for spatial- and time-resolved spectroscopy. J. Synchrotron Radiat. **27**, 695–707 (2020). https://doi.org/10.1107/S1600577520004440
16. R.A. House, J.J. Marie, M.A. Pérez-Osorio et al., The role of O_2 in O-redox cathodes for Li-ion batteries. Nat. Energy **6**, 781–789 (2021). https://doi.org/10.1038/s41560-021-00780-2
17. V. Bisogni, S. Catalano, R.J. Green et al., Ground-state oxygen holes and the metal-insulator transition in the negative charge-transfer rare-earth nickelates. Nat. Commun. **7**, 13017 (2016). https://doi.org/10.1038/ncomms13017
18. L. Kjellsson, K.D. Nanda, J.E. Rubensson et al., Resonant inelastic X-ray scattering reveals hidden local transitions of the aqueous OH radical. Phys. Rev. Lett. **124**, 236001 (2020). https://doi.org/10.1103/PhysRevLett.124.236001
19. R.N. Aljawfi, M. Abu-Samak, S. Kumar et al., Explore the charge transfer and d-d excitation in perovskite manganite using 2p3d resonant inelastic x-ray scattering. J. Alloy. Compd. **904**, 164020 (2022). https://doi.org/10.1016/j.jallcom.2022.164020
20. M.L. Baker, M.W. Mara, J.J. Yan et al., K- and L-edge x-ray absorption spectroscopy (XAS) and resonant inelastic x-ray scattering (RIXS) determination of differential orbital covalency (DOC) of transition metal sites. Coordin. Chem. Rev. **345**, 182–208 (2017). https://doi.org/10.1016/j.ccr.2017.02.004
21. H. Suzuki, H. Liu, J. Bertinshaw et al., Proximate ferromagnetic state in the Kitaev model material α-RuCl3. Nat. Commun. **12**, 4512 (2021). https://doi.org/10.1038/s41467-021-24722-4
22. C.T. Parzyck, N.K. Gupta, Y. Wu et al., Absence of $3a_0$ charge density wave order in the infinite-layer nickelate $NdNiO_2$. Nat. Mater. **23**, 440 (2024). https://doi.org/10.1038/s41563-024-01832-0
23. D.G. Hawthorn, F. He, L. Venema et al., An in-vacuum diffractometer for resonant elastic soft X-ray scattering. Rev. Sci. Instrum. **82**, 073104 (2011). https://doi.org/10.1063/1.3607438
24. H. Liu, J. Cao, Y. Wang et al., Soft x-ray spectroscopic endstation at beamline 08U1A of Shanghai Synchrotron Radiation Facility. Rev. Sci. Instrum. **90**, 043103 (2019). https://doi.org/10.1063/1.5080760
25. C.P. Wang, Z.J. Xu, H.G. Liu et al., Soft x-ray ptychography method at SSRF. Nucl. Sci. Tech. **28**, 74 (2017). https://doi.org/10.1007/s41365-017-0227-6
26. R.Z. Tai, Z. Zhao, Commissioning and first results of the SSRF phase-II beamline project. J. Phys. Conf. Ser. **2380**, 012004 (2023). https://doi.org/10.1088/1742-6596/2380/1/012004
27. Y. Chen, C. Chen, C. Zheng et al., Database of ab initio L-edge x-ray absorption near edge structure. Scientific Data **8**, 153 (2021). https://doi.org/10.1038/s41597-021-00936-5
28. P. Ildefonse, D. Cabaret, P. Sainctavit et al., Aluminium X-ray absorption near edge structure in model compounds and Earth's surface minerals. Phys. Chem. Miner. **25**, 112–121 (1998). https://doi.org/10.1007/s002690050093
29. J. Li, Y. Zou, Z. Chen et al., Ionization chamber based on multichannel plate and its application on synchrotron radiation. Nuclear Techniques **39**, 050101 (2016). https://doi.org/10.11889/j.0253-3219.2016.hjs.39.050101
30. L. Xue, R. Reininger, Y.Q. Wu et al., Design of an ultrahigh-energy-resolution and wide-energy-range soft x-ray beamline. J. Synchrotron Radiat. **21**, 273–279 (2014). https://doi.org/10.1107/S1600577513029093
31. G.C. King, M. Tronc, F.H. Read et al., An investigation of the structure near the $L_{2,3}$ edges of argon, the $M_{4,5}$ edges of krypton and the $N_{4,5}$ edges of xenon, using electron impact with high resolution. J. Phys. B P. Soc Photo-Opt Ins. **10**, 2479 (1977). https://doi.org/10.1088/0022-3700/10/12/026
32. V.N. Strocov, T. Schmitt, U. Flechsig et al., High-resolution soft x-ray beamline ADRESS at the Swiss Light Source for resonant inelastic x-ray scattering and angle-resolved photoelectron spectroscopies. J. Synchrotron Radiat. **17**, 631–643 (2010). https://doi.org/10.1107/S0909049510019862
33. R.R. Blyth, R. Delaunay, M. Zitnik et al., The high resolution gas phase photoemission beamline. Elettra. J. Electron Spectrosc. **101–103**, 959–964 (1999). https://doi.org/10.1016/S0368-2048(98)00381-8
34. X. Meng, Z. Guo, Y. Wang et al., Design and performance of bending-magnet beamline BL02B at the SSRF. J. Synchrotron Radiat. **26**, 543–550 (2019). https://doi.org/10.1107/S1600577518018179
35. T. Schmitt, V.N. Strocov, K.J. Zhou et al., High-resolution resonant inelastic x-ray scattering with soft x-rays at the ADRESS beamline of the Swiss light source: instrumental developments and scientific highlights. J. Electron Spectrosc. **188**, 38–46 (2013). https://doi.org/10.1016/j.elspec.2012.12.011
36. V.N. Strocov, T. Schmitt, U. Flechsig et al., Numerical optimization of spherical variable-line-spacing grating x-ray spectrometers. J. Synchrotron Radiat. **18**, 134–142 (2011). https://doi.org/10.1107/S0909049510054452
37. S. Wendt, P. Sprunger, E. Lira et al., The role of interstitial sites in the Ti3d defect state in the band gap of titania. Science **320**, 1755–1759 (2008). https://doi.org/10.1126/science.1159846
38. Y. Shao, C. Kuo, X. Feng et al., Interface carriers and enhanced electron-phonon coupling effect in Al_2O_3/TiO_2 heterostructure revealed by resonant inelastic soft x-ray scattering. Adv. Funct. Mater. **31**, 2104430 (2021). https://doi.org/10.1002/adfm.202104430
39. J. Zhou, H. Fang, J. Maley et al., Electronic structure of TiO_2 nanotube arrays from X-ray absorption near edge structure studies. J. Mater. Chem. **19**, 6804 (2009). https://doi.org/10.1039/B909225K
40. W. Zhong, M. Zhang, G. Freychet et al., Decoupling complex multi-length-scale morphology in non-fullerene photovoltaics with nitrogen K-edge resonant soft x-ray scattering. Adv. Mater. **34**, 2107316 (2022). https://doi.org/10.1002/adma.202107316
41. J. Fink, E. Schierle, E. Weschke et al., Resonant elastic soft X-ray scattering. Rep. Prog. Phys. **76**, 056502 (2013). https://doi.org/10.1088/0034-4885/76/5/056502
42. D.G. Hawthorn, K.M. Shen, J. Geck et al., Resonant elastic soft X-ray scattering in oxygen-ordered $YBa_2Cu_3O_6$. Phys. Rev. B **84**, 075125 (2011). https://doi.org/10.1103/PhysRevB.84.075125
43. Y.D. Chuang, W.S. Lee, Y.F. Kung et al., Real-time manifestation of strongly coupled spin and charge order parameters in stripe-ordered $La_{1.75}$ $Sr_{0.25}$ NiO_4 nickelate crystals using time-resolved resonant X-ray diffraction. Phys. Rev. Lett. **110**, 127404 (2013). https://doi.org/10.1103/PhysRevLett.110.127404
44. W.S. Lee, Y.D. Chuang, R.G. Moore et al., Phase fluctuations and the absence of topological defects in a photo-excited charge-ordered nickelate. Nat. Commun. **3**, 838 (2012). https://doi.org/10.1038/ncomms1837